AGU PUBLICATIONS

Geophysical Research Letters

RESEARCH LETTER
10.1002/2014GL062097

Key Points:
- New constraints on a ULVZ provide a 1:1 V_S:V_P ratio
- The 1:1 ratio indicates a compositional origin to the ULVZ
- ULVZ composition may be Fe-enriched ferropericlase

Supporting Information:
- Figures S1–S7 and equations (S1)–(S7)

Correspondence to:
M. S. Thorne,
michael.thorne@utah.edu

Citation:
Brown, S. P., M. S. Thorne, L. Miyagi, and S. Rost (2015), A compositional origin to ultralow-velocity zones, *Geophys. Res. Lett.*, *42*, doi:10.1002/2014GL062097.

Received 3 OCT 2014
Accepted 9 JAN 2015
Accepted article online 14 JAN 2015

A compositional origin to ultralow-velocity zones

Samuel P. Brown[1], Michael S. Thorne[1], Lowell Miyagi[1], and Sebastian Rost[2]

[1]Department of Geology and Geophysics, University of Utah, Salt Lake City, Utah, USA, [2]School of Earth and Environment, University of Leeds, Leeds, UK

Abstract We analyzed vertical component short-period *ScP* waveforms for 26 earthquakes occurring in the Tonga-Fiji trench recorded at the Alice Springs Array in central Australia. These waveforms show strong precursory and postcursory seismic arrivals consistent with ultralow-velocity zone (ULVZ) layering beneath the Coral Sea. We used the Viterbi sparse spike detection method to measure differential travel times and amplitudes of the postcursor arrival *ScSP* and the precursor arrival *SPcP* relative to *ScP*. We compare our measurements to a database of 340,000 synthetic seismograms finding that these data are best fit by a ULVZ model with an *S* wave velocity reduction of 24%, a *P* wave velocity reduction of 23%, a thickness of 8.5 km, and a density increase of 6%. This 1:1 V_S:V_P velocity decrease is commensurate with a ULVZ compositional origin and is most consistent with highly iron enriched ferropericlase.

1. Introduction

A salient feature of the core-mantle boundary (CMB) region is the existence of ultralow-velocity zones (ULVZs). ULVZs have been detected using many seismic phases, including *SPdKS* [e.g., *Thorne and Garnero*, 2004], *PcP* [e.g., *Mori and Helmberger*, 1995], *ScP* [e.g., *Garnero and Vidale*, 1999], *ScS* [*Avants et al.*, 2006], *PKP* precursors [e.g., *Vidale and Hedlin*, 1998], and anomalies in travel time or slowness of a variety of different phases [e.g., *Xu and Koper*, 2009]. These studies show that ULVZs are characterized by a wide range of elastic parameters. For example, *S* wave velocity reductions (δV_S) have been reported as large as 45% (all percentages reported with respect to the Preliminary Reference Earth Model (PREM) [*Dziewonski and Anderson*, 1981]), *P* wave velocity reductions (δV_P) as large as 20%, density increases ($\delta\rho$) of up to 10%, and thicknesses of up to 40 km (see *Thorne and Garnero* [2004] for a review). Nevertheless, strong trade-offs typically exist in the model space [e.g., *Garnero and Helmberger*, 1998], and many of these parameters are uncertain.

Of the elastic parameters, the *P* wave velocity reduction is the most well constrained parameter. The seismic phase *SPdKS* is primarily sensitive to the *P* wave velocity reduction at the base of the mantle [see, e.g., *Rondenay et al.*, 2010]. In the southwest Pacific Ocean region, *P* wave velocity reductions of 10 to 15% are well constrained [*Thorne et al.*, 2013; *Zhang et al.*, 2009] in at least one ULVZ. Density contrast is less certain, with one study providing a constraint of $10 \pm 5\%$ in a ULVZ beneath the Coral Sea [*Rost et al.*, 2005] and another study providing density constraints in ULVZs beneath the Philippine Islands from 5–10% and 20–25% [*Idehara*, 2011]. The *S* wave velocity reduction appears quite variable, with one study demonstrating an *S* wave velocity reduction of roughly 7% beneath the central Pacific using postcursors to the *ScS* phase [*Avants et al.*, 2006], while *Idehara et al.* [2007] examined *ScP* postcursors beneath the Philippine Sea to show that the *S* wave velocity decrease must be at least 20%. Additional evidence beneath the Coral Sea from *ScP* arrivals shows an *S* wave velocity decrease of 24% [*Rost et al.*, 2006]. Due to the trade-off between *P* wave velocity, *S* wave velocity, and thickness, it is difficult to determine the ULVZ elastic parameters precisely. Nonetheless, constraining these parameters is paramount in determining what ULVZs physically represent.

The seismic phase *ScP* is of utmost importance in studying ULVZs as it is sensitive to all elastic parameters [*Garnero and Vidale*, 1999]. *ScP* is an *S* wave that converts to a *P* wave at its reflection on the CMB. Figure 1a shows the *ScP* raypath through the mantle, with the direct *P* wave path for comparison. The reason *ScP* is well suited for ULVZ studies is because of the existence of at least two precursors and one postcursor that are predicted if the *ScP* wavefield interacts with a ULVZ. These additional phases (Figure 1b) are (1) *SdP*—a precursor occurring from the reflection off the top of the ULVZ, (2) *SPcP*—a precursor occurring when the downgoing *S* wave converts to a *P* wave at the top of the ULVZ, and (3) *ScSP*—a postcursor that occurs when the upgoing *ScS* wave converts to a *P* wave at the top of the ULVZ. A synthetic seismogram showing the predicted *ScP* waveform for the PREM model is compared to the predicted waveform for a model including a

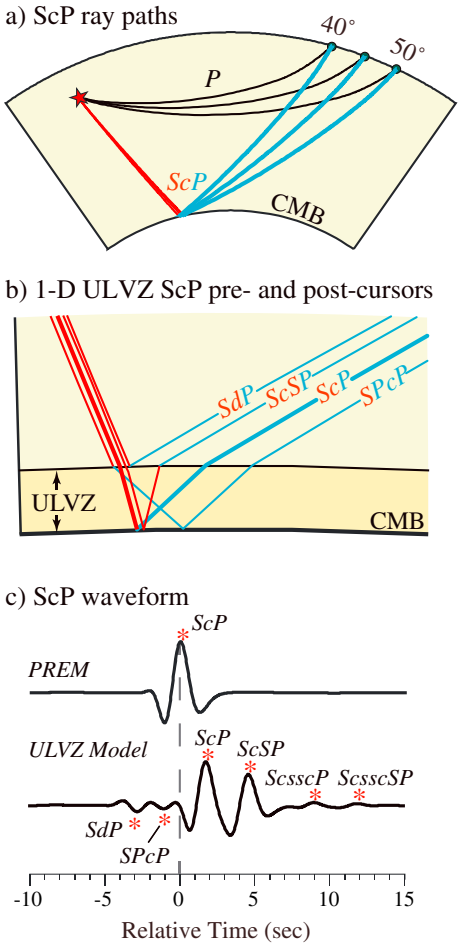

Figure 1. (a) Direct *P* wave (black) and *ScP* rays are shown at epicentral distances of 40°, 45°, and 50°. (b) Detail of raypaths near the core-mantle boundary for precursory and postcursory rays associated with a ULVZ. Raypaths are drawn for a ULVZ model with thickness = 20 km, $\delta V_S = -30\%$, and $\delta V_P = -10\%$. Rays are color coded red and blue for the *S* and *P* legs of the raypaths, respectively. (c) Vertical component displacement synthetic seismograms calculated for the PREM (Figure 1c, top) and ULVZ (Figure 1c, bottom) models. The ULVZ model is the same as for which rays are drawn in Figure 1b. Seismograms are aligned at zero time on the PREM *ScP* arrival. In addition to the arrivals drawn in Figure 1b, additional reverberations inside the ULVZ are also observed—phases labeled *ScsscP* and *ScsscSP*. Raypaths and synthetics in Figures 1b and 1c are calculated for an epicentral distance of 45°.

1-D ULVZ in Figure 1c. Additional reverberations within the ULVZ, phases labeled *ScsscP* and *ScsscSP* in Figure 1c, can be observed in synthetics yet are typically too low amplitude to be observed in the data.

The value of *ScP* in determining the *S* wave velocity reduction is that the amplitudes of the *SdP* and *ScSP* arrivals are most strongly dependent on the *S* wave velocity reduction [*Rost and Revenaugh*, 2003]. However, precise determination of the amplitudes of the *ScSP* postcursor is complicated by the presence of the *ScP* coda, which is most pronounced in the short-period data. Additionally, both of the precursor arrivals are predicted to have relatively low amplitudes with respect to *ScP* (see Figure 1c), and the majority of studies have only identified a single precursor due to the interference of the two low-amplitude phases [e.g., *Rost et al.*, 2005]. In this paper we examine *ScP* waveforms interacting with a known ULVZ in the southwestern Pacific Ocean region [*Rost et al.*, 2005, 2006]. We use the Viterbi sparse spike detection (VSSD) method [*Brown and Thorne*, 2013] to accurately determine differential travel times and amplitude ratios for *ScP* precursor and postcursor arrivals. We compare this set of measurements to synthetic predictions constraining *S* and *P* wave velocity reductions in a single ULVZ.

2. *ScP* Data and Viterbi Sparse Spike Detection Method

We analyze a data set of *ScP* records from 26 earthquakes in the Fiji-Tonga area recorded at the Alice Springs Array located in central Australia. Individual records were band-pass filtered between 1 and 4 Hz and beamformed on the *ScP* arrival to provide a single high signal-to-noise ratio trace for each event (see *Rost et al.* [2006] for the details on event beams, event locations, and bouncepoint location). These events provide a tight cluster of *ScP* bounce points (roughly 30 km × 30 km) on the CMB centered at 167.5°E longitude and 25°S latitude, spanning an epicentral distance range from 40.9° to 42.8°. *Rost et al.* [2006] identified a precursor (arriving 1.9 s prior to the *ScP* arrival) identified as the *SdP* arrival. An *SPcP* precursor and *ScSP* postcursor are also apparent in these data; yet these arrivals are partially masked by destructive interference from the *ScP* arrival.

We use the Viterbi sparse spike detection (VSSD) technique [*Brown and Thorne*, 2013] to search for *ScP* precursor and postcursor directly in the recorded traces while simultaneously obtaining estimates of their relative amplitudes and differential travel times. Given an approximate source time function, the VSSD method provides a statistically robust way to search a predefined set of spike trains for the best nonlinear fit to a composite waveform, accounting for Gaussian distributed random noise, errors in the source time function, and constructive/destructive interference between closely spaced arrivals. A synthetic trace is built for each candidate spike train through convolution with the source time function. A profile hidden Markov model (HMM) [*Eddy*, 1995] is built for each synthetic trace. The profile HMM represents a stochastic model for generating synthetic waveforms, the most likely of

which will be the synthetic upon which the model is based. The model consists of a linear array of match states, where each match state corresponds to a sample in the synthetic seismogram, and is characterized by a Gaussian distribution centered on the synthetic sample amplitude. The linear topology is augmented with insert and delete states between match states, which allow the waveforms to contract and dilate, facilitating nonlinearity in waveform alignments. The Viterbi algorithm [*Viterbi*, 1967] is applied to find the optimal nonlinear alignment between a data trace and the profile HMM. This optimal alignment represents the path through the HMM, which generates the data trace with the highest probability. The optimal path, π^*, is the state sequence which optimizes the following equation:

$$P^{\pi}(\text{Data}|\text{Model}) = \prod_i a_{kl}^{\pi} g_l^{\pi}(d_i), \tag{1}$$

where i is a sample index for the data trace, d_i is a sample of the data trace, a_{kl} is a transition probability associated with transitioning from state k to l, and g_l is a Gaussian distribution associated with each sample amplitude in the synthetic model. The state integer π represents a specific state sequence that determines the values of k and l. A log-odds score S is assigned to each profile HMM, based on the optimal alignment to a data trace:

$$S(\text{Data}|\text{Model}) = \log\left(\frac{P(\text{Data}|\text{Model})}{P(\text{Data}|W)}\right), \tag{2}$$

where W is a white noise model. The log-odds score is a ratio of the likelihood of a given model producing a given data trace over the likelihood of a white noise model producing the data trace. Travel times and amplitudes for each individual arrival in a complex waveform are derived from the highest scoring model. Relative amplitudes are taken directly from the spike train from which the model was built, and differential travel times are adjusted based on the optimal alignment.

We create an empirical source, between 2 and 3 s in length, composed of a windowed and tapered direct *P* wave arrival for each event (Figure 2a). The direct *P* wave arrival was too noisy to provide a suitable source time function estimate for 10 of the 26 events, which led to their exclusion from this analysis. The *ScP* arrival travels a longer path through the mantle and is more attenuated than the *P* wave arrival. Thus, the frequency content of our empirical source is slightly higher than for the *ScP* arrival, but this variation in frequency content is accommodated for by the VSSD method [*Brown and Thorne*, 2013].

3. Results

Figure 2a shows an example where we search for multiple (1 to 6) arrivals in a beamed trace from a single event recorded at Alice Springs Seismic Array using the VSSD method. When only one arrival is searched for, the algorithm finds the *ScP* arrival. When we search for two arrivals, we recover the *ScSP* arrival, the next highest-amplitude arrival after *ScP*. The third arrival finds an additional postcursor, and the fourth arrival finds the *SPcP* precursor. Looking for five and six arrivals does not reveal a consistent *SdP* arrival, and the increase in log likelihood score starts to flatten. Additionally, the amplitude of arrivals greater than four becomes increasingly lower and within the noise level; thus, we expect that no more than four arrivals can consistently be determined in these data. The overall data fit increases when searching for five or six arrivals but does not significantly influence the travel time or amplitude of the arrivals already determined, and we hence limit our search to the five largest amplitude arrivals in the *ScP* wavefield for the events in our data set.

Figure 2b shows VSSD alignments and picks for the 16 events analyzed. The inclusion of the postcursor beyond *ScSP* is necessary to get a good waveform fit for *ScSP*. This additional postcursor is possibly a diffracted arrival off the far edge of the ULVZ and is too large amplitude to be consistent with one of the ULVZ reverberations shown in Figure 1c. Figure 3a shows the differential travel times versus relative amplitudes for all 16 events. The average *ScP-SPcP* differential travel time is 0.9094 ± 0.0455 s, and the average *ScSP-ScP* time is 0.8625 ± 0.0806 s. Average amplitude ratios are $SPcP/ScP = -0.2555 \pm 0.0671$ and $ScSP/ScP = 0.5073 \pm 0.1448$.

Synthetic seismograms are computed using the generalized ray method (GRM) [*Helmberger*, 1983]. We use the PREM background model with a 1-D ULVZ model embedded at the base of the mantle. Synthetic seismograms are computed for a 500 km deep event at an epicentral distance of 42°. We used the GRM in order to model individual arrivals obtaining a spike train similar to those obtained using the VSSD technique. We compute synthetic seismograms where we allow the following ULVZ parameters to vary: (1) δV_S decreases from 0% to 50% in 1% increments, (2) δV_P decreases from 0% to 30% in 1% increments, (3) $\delta\rho$ variations from

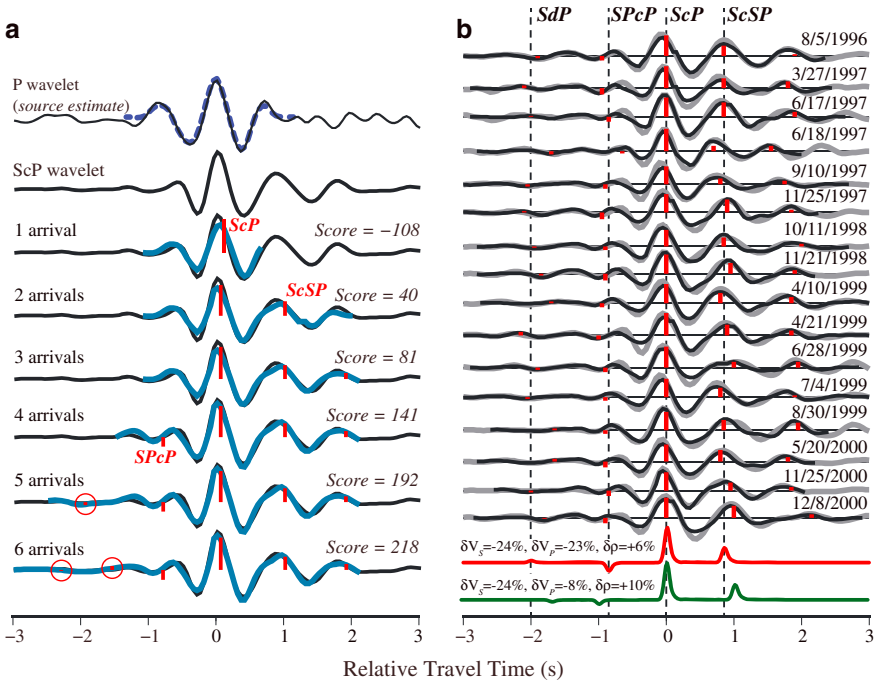

Figure 2. (a) Analysis of a single event occurring on 25 November 2000. The top trace (black line) shows the direct *P* wave. The dashed blue line shows the windowed *P* wavelet used as the source time function estimate. The second trace from the top (heavy black line) shows the raw *ScP* wavelet which is repeated for each trace below. Each subsequent trace shows the best fit VSSD solution for this event using 1 through 6 arrivals. In each case, the red spike shows the best fit amplitude and travel time for the number of arrivals being fit. The light blue trace is an overlay of the source time function convolved with the best fit spike train. The log-odds score is shown to the right for each fit. Because the amplitudes for arrivals 5 and 6 are low, we have highlighted their positions with red circles. (b) Travel time and amplitude picks (red spikes) computed by the VSSD method for the 16 events analyzed in this study are shown. The beam-formed *ScP* trace for each event is shown as the gray trace. The VSSD-derived waveforms are overlain (black traces). The lowermost two traces are GRM synthetic predictions convolved with a 0.25 s dominant period source time function at an epicentral distance of 42°. The red trace is for a ULVZ model with $\delta V_S = -24\%$, $\delta V_P = -23\%$, thickness = 8.5 km, and density = +6%, and the green trace is for a ULVZ model with $\delta V_S = -24\%$, $\delta V_P = -8\%$, thickness = 8.5 km, and density = +10%.

−10% to 20% in 1% increments, and (4) ULVZ thickness (h) from 1 to 20 km in 1 km increments. In total, we have a database of synthetic seismograms for nearly 340,000 ULVZ models.

In order to characterize the likelihood of models from the suite of synthetics, four Gaussian probability mass functions were defined from the means and variances of the measured differential travel times and relative amplitudes. Figure 3b shows $P_1\ (\partial V_S, \partial V_P)$, the likelihood of models considering only differential travel times and amplitudes of *ScSP* relative to *ScP*, which we define as

$$P_1\ (\partial V_S, \partial V_P) = \text{argmax}_h(< P_{aScSP}(\partial V_S, \partial V_P, \delta\rho, h) * P_{tScSP}(\partial V_S, \partial V_P, \delta\rho, h) >), \quad (3)$$

where h denotes ULVZ thickness, $P_{aScSP}(\partial V_S, \partial V_P, \delta\rho, h)$ is the probability assigned to the *ScSP*/*ScP* differential amplitude for a given synthetic model, $P_{tScSP}(\partial V_S, \partial V_P, \delta\rho, h)$ is the probability assigned to the *ScSP*-*ScP* differential travel time, and $<>$ denotes an ensemble average over density variations. Examination of Figure 3b demonstrates that the *ScSP* postcursor provides a strong constraint on δV_S, giving an approximate value of −25%, which is consistent with the *Rost et al.*'s [2006] estimate of δV_S.

Figure 3c shows $P_2\ (\partial V_S, \partial V_P)$, the likelihood of models considering differential travel times and amplitudes of both *ScSP* and *SPcP* relative to *ScP*, which we define as

$$P_2\ (\partial V_S, \partial V_P) = \text{argmax}_h \begin{pmatrix} < P_{aScSP}(\partial V_S, \partial V_P, \delta\rho, h) * P_{tScSP}(\partial V_S, \partial V_P, \delta\rho, h) * \\ P_{aSPcP}(\partial V_S, \partial V_P, \delta\rho, h) * P_{tSPcP}(\partial V_S, \partial V_P, \delta\rho, h) > \end{pmatrix}, \quad (4)$$

where $P_{aSPcP}(\partial V_S, \partial V_P, \delta\rho, h)$ is the probability assigned to the *SPcP*/*ScP* differential amplitude for a given synthetic model, $P_{tSPcP}(\partial V_S, \partial V_P, \delta\rho, h)$ is the probability assigned to the *ScP*-*SPcP* differential travel time pick.

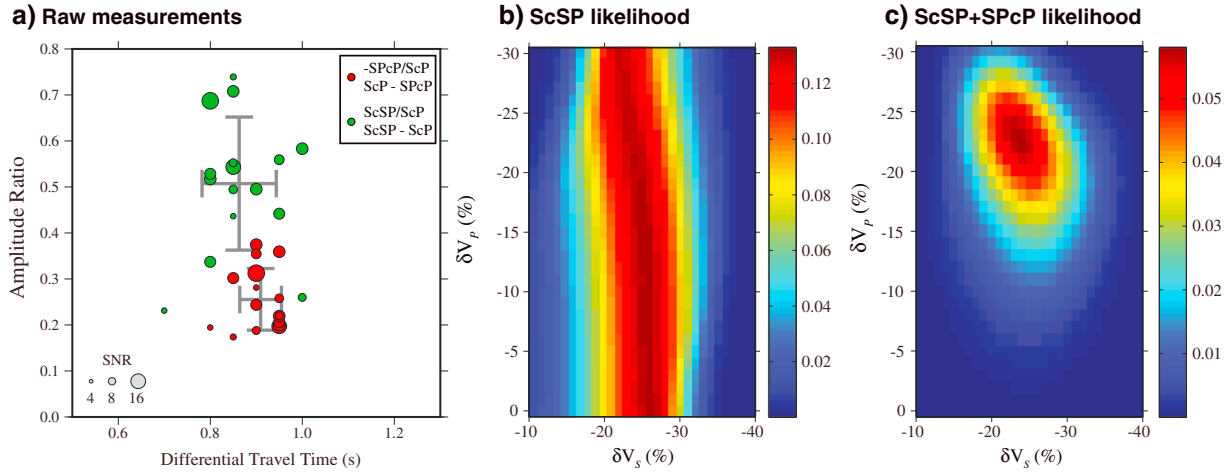

Figure 3. (a) VSSD measured differential travel times versus relative amplitudes. The red circles show *ScP-SPcP* and $-$*SPcP/ScP* differentials, whereas the green circles show the *ScSP-ScP* and *ScSP/ScP* differentials. The gray crosses show the average and 1σ error bars for the measurements. The size of the circles is scaled by the signal-to-noise ratio of the *ScP* beam. (b) Velocity variation likelihood, constrained only by *ScSP* travel times and amplitudes. (c) Velocity variation likelihood, constrained by *ScSP* and *SPcP* travel times and amplitudes.

We see a clear peak in the likelihood plot (Figure 3c) located at $\delta V_P = -23\%$ and $\delta V_S = -24\%$. The most likely individual model is given by

$$P_3 = \max\begin{pmatrix} P_{aScSP}(\partial V_S, \partial V_P, \delta\rho, h) * P_{tScSP}(\partial V_S, \partial V_P, \delta\rho, h)^* \\ P_{aSPcP}(\partial V_S, \partial V_P, \delta\rho, h) * P_{tSPcP}(\partial V_S, \partial V_P, \delta\rho, h) \end{pmatrix} \quad (5)$$

This provides a best fit model with the following parameters: $\delta V_S = -24\%$, $\delta V_P = -23\%$, $\delta\rho = +6\%$, and $h = 8.5$ km. The synthetic seismogram for this best fit model is shown in Figure 2b. The additional information from *SPcP* resolves the ambiguity between δV_P and h. Density variation within the ULVZ is the least well constrained of the elastic parameters and does not lead to a significant change in model probability over the range of density variations tested.

4. Discussion and Conclusions

The results of *Rost et al.* [2006] fit synthetic waveforms and determined a best fit model of $\delta V_S = -24\%$, $\delta V_P = -8\%$, $\delta\rho = +10\%$, and $h = 8.5$ km, which we will refer to as the *partial-melt model* due to its 3:1 V_S:V_P ratio. A synthetic for this model is also shown in Figure 2b. There is not a large amount of difference in amplitude or travel time for the *SPcP* and *ScSP* arrivals for these different predictions. Yet the partial-melt model predicts a negative polarity *SdP* arrival, whereas our best fit model predicts a positive polarity *SdP* arrival. We are not able to constrain amplitude or travel time of the *SdP* arrival in our individual event beams. We further apply the VSSD technique to a trace created by forming a double beam of all events in order to further enhance an *SdP* arrival. However, the *SdP* arrival is within the noise level, and the polarity of the *SdP* arrival cannot be constrained (see supporting information); hence, the partial-melt model cannot be entirely ruled out.

The origins of ULVZs have been suggested to be due to a variety of causes including a metal-bearing layer [*Manga and Jeanloz*, 1996], iron-enriched postperovskite [*Mao et al.*, 2006], iron enrichment of ferropericlase (Fp) [*Wicks et al.*, 2010], and partial melt [*Berryman*, 2000; *Labrosse et al.*, 2007; *Williams and Garnero*, 1996]. Of these scenarios, partial melt has received the most attention. This partial-melt origin for ULVZs predicts a 3:1 ratio for reduction of V_S:V_P wave speeds [*Williams and Garnero*, 1996], which is incompatible with our most likely model which has a 1:1 ratio. This reduction is consistent with compositional or mineralogical variations, and thus, we explore these scenarios.

Using elastic properties and densities available in the literature, we calculate changes in velocity and density for several mineralogical models at conditions of 136 GPa and 3500 K. Since the detailed mineralogical and chemical composition at the base of the mantle is uncertain, rather than attempt to model a complete mineralogical mixture, we perform a computation where the mineral phase of interest is mixed with PREM

velocities and densities [*Wicks et al.*, 2010]. We explore possible enrichment of Fp with 35% Fe (Fp35) [*Chen et al.*, 2012], Fp with 84% Fe (Fp84) [*Wicks et al.*, 2010], hexagonal close packed Fe [*Lin et al.*, 2005], $FeSiO_3$ postperovskite [*Stackhouse and Brodholt*, 2008], Fe_2O_3 postperovskite [*Stackhouse and Brodholt*, 2008], $FeSiO_3$ perovskite [*Stackhouse et al.*, 2006], and B2 structured FeSi [*Caracas and Wentzcovitch*, 2004; *Ono*, 2013; *Vočadlo et al.*, 2002]. We find that 25–30% enrichment of Fp84 is the only model tested that provides a decrement ratio of 1:1 with a 23% decrease in velocities and a 6% increase in density. Notably, Fp35 does not provide a 1:1 decrease at these velocity reductions, which implies that very high Fe content is required (i.e., in excess of 35% substitution). Thus, our seismic data are most consistent with a solid state ULVZ enriched in high Fe content Fp, perhaps even approaching pure wüstite (FeO) end-member composition.

Since it is controversial if temperatures at the base of the mantle are hot enough to induce significant melting of mantle material [*Andrault et al.*, 2011], and because our observations are incompatible with partial melt, we propose a mechanism that does not require melting of mantle material. In this mechanism, ULVZs are formed through entrainment of core material followed by chemical reaction and gravitational settling. This mechanism can explain observations for the formation of solid state (1:1) and partially molten (3:1) ULVZs. When Fp is in contact with molten Fe, a morphological instability occurs, allowing liquid iron droplets to penetrate deep into Fp, providing a mechanism for entrainment of core material into the mantle [*Otsuka and Karato*, 2012]. Liquid Fe has a very high affinity for oxygen, so it is expected that liquid Fe should "strip" oxygen away from the surrounding mantle material [*Asahara et al.*, 2007]. As this Fe-enriched material percolates upward from the core-mantle boundary, the steep geotherm in this region is likely to cause precipitation of solid material. We expect that since the amount of Fe drawn out of the core is relatively small compared to the volume of the surrounding mantle [*Otsuka and Karato*, 2012], the Fe droplets should become highly enriched in oxygen. If there is sufficient oxygen enrichment, the material lies on the oxygen-rich side of the Fe-FeO eutectic, pure solid FeO will precipitate [*Seagle et al.*, 2008]. Reactions between liquid Fe and mantle silicates to form FeO and FeSi have been documented in high pressure-temperature experiments [e.g., *Knittle and Jeanloz*, 1989]. If FeSi is produced by such a reaction [*Knittle and Jeanloz*, 1989], and it has a lower melting temperature than Fe [e.g., *Santamaría-Pérez and Boehler*, 2008], it should remain in the molten state, likely alloyed with the molten Fe droplets. This residual molten FeSi alloy will be denser than mantle silicate [*Caracas and Wentzcovitch*, 2004] and may eventually drain back to the core in the liquid state but may temporarily form partially molten ULVZs. Percolation of Fe droplets into the mantle is strongly temperature controlled [*Otsuka and Karato*, 2012], and we expect that this process is broadly occurring across the CMB. However, in hotter regions (e.g., near Large Low Shear Velocity Provinces (LLSVPs)), this process will be more efficient. Localized regions of Fe percolation could also give rise to temporary partially molten ULVZs. However, as the Fe reacts with silicate mantle, FeO collection at the base of the mantle will occur. *McNamara et al.* [2010] have shown that a dense ULVZ-like layer will get swept toward the edges of LLSVPs. Hence, FeO-rich ULVZs may pile up into ULVZs observed at LLSVP boundaries.

Acknowledgments

We gratefully acknowledge the University of Utah Center for High Performance Computing for the computer resources and support. M.T. and S.B. were partially supported by NSF grant EAR-1014749. S.R. was partially supported by NERC grant NE/H022473/1. L.M. was partially supported by NSF grant EAR-1344579. L.M. would like to thank Zhixue Du for the helpful discussions. Figures were drawn using the Generic Mapping Tools [*Wessel and Smith*, 1998]. Data used in this study may be downloaded from http://web.utah.edu/thorne/pubs.html.

The Editor thanks an anonymous reviewer for assisting in the evaluation of this paper.

References

Andrault, D., N. Bolfan-Casanova, G. Lo Nigro, M. A. Bouhifd, G. Garbarino, and M. Mezouar (2011), Solidus and liquidus profiles of chondritic mantle: Implication for melting of the Earth across its history, *Earth Planet. Sci. Lett.*, *304*, 251–259, doi:10.1016/j.epsl.2011.02.006.

Asahara, Y., D. J. Frost, and D. C. Rubie (2007), Partitioning of FeO between magnesiowüstite and liquid iron at high pressures and temperatures: Implications for the composition of the Earth's outer core, *Earth Planet. Sci. Lett.*, *257*, 435–449, doi:10.1016/j.epsl.2007.03.006.

Avants, M., T. Lay, and E. J. Garnero (2006), A new probe of ULVZ *S* wave velocity structure: Array stacking of *ScS* waveforms, *Geophys. Res. Lett.*, *33*, L07314, doi:10.1029/2005GL024989.

Berryman, J. G. (2000), Seismic velocity decrement ratios for regions of partial melt in the lower mantle, *Geophys. Res. Lett.*, *27*(3), 421–424, doi:10.1029/1999GL008402.

Brown, S. P., and M. S. Thorne (2013), Viterbi sparse spike detection, *Geophysics*, *78*(4), V157–V169, doi:10.1190/GEO2012-0209.1.

Caracas, R., and R. M. Wentzcovitch (2004), Equation of state and elasticity of FeSi, *Geophys. Res. Lett.*, *31*, L20603, doi:10.1029/2004GL020601.

Chen, B., J. M. Jackson, W. Sturhahn, D. Zhang, J. Zhao, J. K. Wicks, and C. A. Murphy (2012), Spin crossover equation of state and sound velocities of $(Mg_{0.65}Fe_{0.35})O$ ferropericlase to 140 GPa, *J. Geophys. Res.*, *117*, B08208, doi:10.1029/2012JB009162.

Dziewonski, A. M., and D. L. Anderson (1981), Preliminary reference Earth model, *Phys. Earth Planet. Inter.*, *25*, 297–356.

Eddy, S. R. (1995), Multiple alignment using hidden Markov models, in *Proceedings of the Third International Conference Intelligent Systems for Molecular Biology*, pp. 114–120.

Garnero, E. J., and D. V. Helmberger (1998), Further structural constraints and uncertainties of a thin laterally varying ultralow velocity layer at the base of the mantle, *J. Geophys. Res.*, *103*(B6), 12,495–12,509, doi:10.1029/98JB00700.

Garnero, E. J., and J. E. Vidale (1999), *ScP*: A probe of ultralow velocity zones at the base of the mantle, *Geophys. Res. Lett.*, *26*(3), 377–380, doi:10.1029/1998GL900319.

Helmberger, D. V. (1983), Theory and application of synthetic seismograms, in *Earthquakes: Observation, Theory and Interpretation*, edited by H. Kanamori, pp. 173–222, Soc. Ital. di Fis, Bologna.

Idehara, K. (2011), Structural heterogeneity of an ultralow velocity zone beneath the Philippine Islands: Implications for core-mantle chemical interactions induced by massive partial melting at the bottom of the mantle, *Phys. Earth Planet. Inter.*, *184*, 80–90, doi:10.1016/j.pepi.2010.10.014.

Idehara, K., A. Yamada, and D. Zhao (2007), Seismological constraints on the ultralow velocity zones in the lowermost mantle from core-reflected waves, *Phys. Earth Planet. Inter.*, *165*, 25–46, doi:10.1016/j.pepi.2007.07.005.

Knittle, E., and R. Jeanloz (1989), Simulating the core-mantle boundary: An experimental study of high-pressure reactions between silicates and liquid iron, *Geophys. Res. Lett.*, *16*(7), 609–612, doi:10.1029/GL016i007p00609.

Labrosse, S., J. W. Hernlund, and N. Coltice (2007), A crystallizing dense magma ocean at the base of the Earth's mantle, *Nature*, *450*, 866–869, doi:10.1038/nature06355.

Lin, J.-F., W. Sturhahn, J. Zhao, G. Shen, H.-K. Mao, and R. J. Hemley (2005), Sound velocities of hot dense iron: Birch's law revisited, *Science*, *308*, 1892–1894, doi:10.1126/science.1111724.

Manga, M., and R. Jeanloz (1996), Implications of a metal-bearing chemical boundary layer in D″ for mantle dynamics, *Geophys. Res. Lett.*, *23*(22), 3091–3094, doi:10.1029/96GL03021.

Mao, W. L., H.-K. Mao, W. Sturhahn, J. Zhao, V. B. Prakapenka, Y. Meng, J. Shu, Y. Fei, and R. J. Hemley (2006), Iron-rich postperovskite and the origin of ultralow velocity zones, *Science*, *312*, 564–565.

McNamara, A. K., E. J. Garnero, and S. Rost (2010), Tracking deep mantle reservoirs with ultralow velocity zones, *Earth Planet. Sci. Lett.*, *299*, 1–9, doi:10.1016/j.epsl.2010.07.042.

Mori, J., and D. V. Helmberger (1995), Localized boundary layer below the mid-Pacific velocity anomaly identified from a PcP precursor, *J. Geophys. Res.*, *100*(B10), 20,359–20,365, doi:10.1029/95JB02243.

Ono, S. (2013), Equation of state and elasticity of B2-type FeSi: Implications for silicon in the inner core, *Phys. Earth Planet. Inter.*, *224*, 32–37, doi:10.1016/j.pepi.2013.08.009.

Otsuka, K., and S.-I. Karato (2012), Deep penetration of molten iron into the mantle caused by a morphological instability, *Nature*, *429*, 243–246, doi:10.1038/nature11663.

Rondenay, S., V. F. Cormier, and E. M. Van Ark (2010), SKS and SPdKS sensitivity to two-dimensional ultralow velocity zones, *J. Geophys. Res.*, *115*, B04311, doi:10.1029/2009JB006733.

Rost, S., and J. Revenaugh (2003), Small-scale ultralow velocity zone structure imaged by *ScP*, *J. Geophys. Res.*, *108*(B1), 2056, doi:10.1029/2001JB001627.

Rost, S., E. J. Garnero, Q. Williams, and M. Manga (2005), Seismological constraints on a possible plume root at the core-mantle boundary, *Nature*, *435*, 666–669, doi:10.1038/nature03620.

Rost, S., E. J. Garnero, and Q. Williams (2006), Fine-scale ultralow velocity zone structure from high-frequency seismic array data, *J. Geophys. Res.*, *111*, B09310, doi:10.1029/2005JB004088.

Santamaría-Pérez, D., and R. Boehler (2008), FeSi melting curve up to 70 GPa, *Earth Planet. Sci. Lett.*, *265*, 743–747, doi:10.1016/j.epsl.2007.11.008.

Seagle, C. T., D. L. Heinz, A. J. Campbell, V. B. Prakapenka, and S. T. Wanless (2008), Melting and thermal expansion in the Fe-FeO system at high pressure, *Earth Planet. Sci. Lett.*, *265*, 655–665, doi:10.1016/j.epsl.2007.11.004.

Stackhouse, S., and J. P. Brodholt (2008), Elastic properties of the postperovskite phase of Fe_2O_3 and implications for ultralow velocity zones, *Phys. Earth Planet. Inter.*, *170*, 260–266, doi:10.1016/j.pepi.2008.07.010.

Stackhouse, S., J. P. Brodholt, and G. D. Price (2006), Elastic anisotropy of $FeSiO_3$ end-members of the perovskite and postperovskite phases, *Geophys. Res. Lett.*, *33*, L01304, doi:10.1029/2005GL023887.

Thorne, M. S., and E. J. Garnero (2004), Inferences on ultralow velocity zone structure from a global analysis of *SPdKS* waves, *J. Geophys. Res.*, *109*, B08301, doi:10.1029/2004JB003010.

Thorne, M. S., E. J. Garnero, G. Jahnke, H. Igel, and A. K. McNamara (2013), Mega ultralow velocity zone and mantle flow, *Earth Planet. Sci. Lett.*, *364*, 59–67, doi:10.1016/j.epsl.2012.12.034.

Vidale, J. E., and M. A. H. Hedlin (1998), Evidence for partial melt at the core-mantle boundary north of Tonga from the strong scattering of seismic waves, *Nature*, *391*, 682–685.

Viterbi, A. (1967), Error bounds for convolutional codes and an asymptotically optimum decoding algorithm, *IEEE Trans. Inf. Theory*, *13*(2), 260–269.

Vočadlo, L., K. S. Knight, G. D. Price, and I. G. Wood (2002), Thermal expansion and crystal structure of FeSi between 4 and 1173 K determined by time-of-flight neutron powder diffraction, *Phys. Chem. Miner.*, *29*(2), 132–139, doi:10.1007/s002690100202.

Wessel, P., and W. H. F. Smith (1998), New, improved version of Generic Mapping Tools released, *Eos Trans. AGU*, *79*(47), 579.

Wicks, J. K., J. M. Jackson, and W. Sturhahn (2010), Very low sound velocities in iron-rich (Mg,Fe)O: Implications for the core-mantle boundary region, *Geophys. Res. Lett.*, *37*, L15304, doi:10.1029/2010GL043689.

Williams, Q., and E. J. Garnero (1996), Seismic evidence for partial melt at the base of Earth's mantle, *Science*, *273*, 1528–1530.

Xu, Y., and K. D. Koper (2009), Detection of a ULVZ at the base of the mantle beneath the northwest Pacific, *Geophys. Res. Lett.*, *36*, L17301, doi:10.1029/2009GL039387.

Zhang, Y., J. Ritsema, and M. S. Thorne (2009), Modeling the ratios of SKKS and SKS amplitudes with ultralow velocity zones at the core-mantle boundary, *Geophys. Res. Lett.*, *36*, L19303, doi:10.1029/2009GL040030.